

RADIATION SHOCK DYNAMICS IN THE SOLAR CHROMOSPHERE – RESULTS OF NUMERICAL SIMULATIONS

MATS CARLSSON

Institute of Theoretical Astrophysics, P.O.Box 1029 Blindern, N-0315 Oslo, Norway

and

ROBERT F. STEIN

Department of Physics & Astronomy, Michigan State University, East Lansing, MI 48824, USA

Abstract.

We report results from self-consistent non-LTE radiation hydrodynamics simulations of the propagation of acoustic waves through the solar chromosphere.

It is found that enhanced chromospheric emission, which corresponds to an outwardly increasing semi-empirical temperature structure, can be produced by wave motions without any increase in the mean gas temperature. Thus, despite long held beliefs, the sun may not have a classical chromosphere in magnetic field free internetwork regions.

The dynamic formation of continuum radiation is described in some detail. Concepts that work well in static models do not necessarily work in the dynamic chromosphere. The contribution function for the intensity may be bimodal with one peak around $\tau_\nu = 1$ and another at a shock at smaller optical depth. The mean height of formation will then be between those regions and have no relation to either formation region.

Above the photosphere, the source function is so decoupled from the Planck function that variations in intensity can *not* be taken as a proxy for gas temperature variations. The emergent intensity does not show the discontinuous rise signature of shock waves even for the continua formed where the shocks are strong. Even in the photosphere a one-to-one correspondence between intensity variation and gas temperature variation is not possible because of the dependence of the formation height on the opacity and therefore on the temperature.

The modification of velocity amplitude and phase as a function of frequency and depth in the atmosphere is described with a transfer function. This function is found to be rather insensitive to the input velocity field in the photosphere. By using the derived transfer function it is possible to construct piston velocities that give photospheric velocities that match observed Doppler shifts.

The simulations closely match the observed behaviour of CaII H₂V bright grains. The formation of bright grains is described in detail and both the brightness and the wavelength position of the grains are explained. It is found that the grain pattern is completely set by the velocity pattern of the piston. The frequency components around 3 minute periods are found to be most important but with significant modulation of the grain behaviour from the low frequency component of the velocity field. The strength of grains is not directly proportional to the photospheric 3 minute power but a result of interference between many modes.

Key words: Hydrodynamics, Radiative transfer, Shock Waves, Sun: chromosphere

1. Introduction

The solar atmosphere is a dynamic radiating medium and many of its outstanding problems require radiation-hydrodynamics for their investigation. Detailed comparison of the evolution of line profiles observed with high spatial and temporal reso-

lution with self-consistent radiation-hydrodynamic simulations provides a means for developing diagnostics for atmospheric motions.

We have developed a code that is capable of such a self-consistent radiation-hydrodynamic treatment under solar chromospheric conditions with the important radiative transitions treated in non-LTE. Earlier schematic studies using sinusoidal monochromatic driving velocity fields (Carlsson and Stein, 1992) are here expanded to driving velocity fields that reproduce observed Doppler shifts in photospheric lines. These simulations are used to show that the whole concept of a semistatic non-magnetic chromosphere is completely misleading. We also focus on the behaviour of the Ca II line profiles, because new high quality data are now available (see other contributions in these proceedings) and the question as to what drives the appearance of K_2V bright grains has been much debated recently (*e.g.*, Rutten and Uitenbroek, 1991, Rammacher and Ulmschneider, 1992, Rossi *et al.*, 1992).

The layout of the paper is as follows: In section 2 we describe the methods used and in section 3 we describe the results with a detailed analysis of the formation of continuum radiation in section 3.1, the equivalent semi-empirical atmosphere in section 3.2 and the atmospheric transfer function in section 3.3. The formation of H_2V and K_2V bright grains is discussed in section 3.4. The results are discussed in section 4 and the conclusions are given in section 5. Phase relations between intensity and velocity for the calcium lines are discussed in a companion paper.

2. Method

We solve the one-dimensional equations of mass, momentum and energy conservation together with the non-LTE radiative transfer and population rate equations, implicitly on an adaptive mesh. The radiative transfer is treated using Scharmer's method (Scharmer, 1981, Scharmer and Carlsson, 1985, Carlsson, 1986). The advection terms are treated using Van Leer's (1977) second order upwind scheme to ensure stability and monotonicity in the presence of shocks. An adaptive mesh is used (Dorfi and Drury, 1987) in order to resolve the regions where the fluid properties are changing rapidly (such as in shock fronts). The equations are solved implicitly to ensure stability in the presence of radiative energy transfer, and to have the time steps controlled by the rate of change of the variables and not by the Courant time for the smallest zones.

We include 6 level model atoms for hydrogen and singly ionized calcium. Other continua are treated as background continua in LTE, using the Uppsala atmospheres program (Gustafsson, 1973). Our initial atmosphere is in radiative equilibrium without line blanketing above the convection zone (for the processes we consider) and extends 100 km into the convection zone, with a time constant divergence of the convective energy flux (on a column mass scale) calculated with the Uppsala code without line blanketing. Basic quantities for the initial atmosphere are shown in Fig. 1.

Waves are driven through the atmosphere by a piston located at the bottom of the computational domain (100 km below $\tau_{500} = 1$) whose velocity is taken from a 3750 second sequence of Doppler shift observations in an Fe I line at $\lambda 396.68$ nm in the wing of the Ca H-line (Lites *et al.*, 1993). Two procedures have been used to

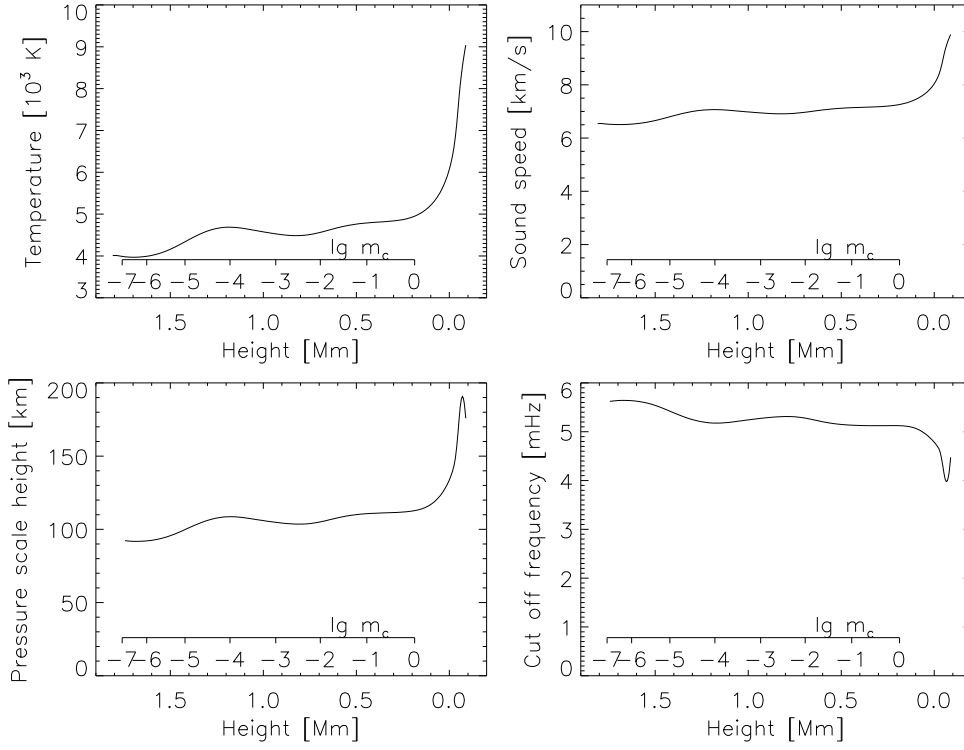


Fig. 1. Temperature, sound speed, pressure scale height and acoustic cut off frequency as functions of height in the starting atmosphere. $\lg(\text{column mass})$ is given as a secondary scale.

transform these observed Doppler shifts into a piston velocity. Originally the Doppler shifts were just scaled with 0.2, which was based on a computed amplification of the amplitude of a monochromatic three-minute wave from the height of the piston to the static height of formation of the iron line (≈ 260 km above $\tau_{500} = 1$). This piston velocity in the simulation produces too little low frequency power at the height of 260 km to give the Doppler shifts observed there. The reason is that the amplification is not constant with frequency, and in addition, there is a zero phase-shift for non-propagating low frequency modes and a non-zero phase-shift at higher frequencies due to the propagation time between the two heights. The second procedure takes these effects into account by using the first simulation to calculate a transfer function, H , for the atmosphere:

$$F[v_{260\text{km}}] = H F[v_{100\text{km}}], \quad (1)$$

where $F[v]$ denotes the Fourier transform of the velocity. The piston velocities are then obtained as

$$v_{\text{piston}} = F^{-1}(H^{-1} F(v_{\text{Fe}})). \quad (2)$$

This procedure gives velocities at 260 km that quite closely match the observed Doppler shifts in the iron line. See Section 3.3 for a discussion of the transfer function of the atmosphere in the simulations.

There is a transmitting boundary condition at the top of the computational domain.

The microturbulence broadening was set to a constant 2 km/s throughout the atmosphere.

After this dynamic calculation is completed, we then recalculate the behavior of the C I, Si I, Mg I and Al I continua in non-LTE. These continua are thus included in the energy balance in the dynamic calculation in LTE and the non-LTE calculation is done for each snap-shot of the dynamic simulation with no back-coupling on the energy balance. The overlap between continua treated in non-LTE is treated iteratively.

The model atoms of C I, Si I, Mg I and Al I are similar to those used in the VAL series of papers (Vernazza, Avrett & Loeser 1973, 1976, 1981) but with the photoionization cross-sections updated with data from Mathisen (1984) and the opacity project (see Seaton *et al.*, 1994 and references therein). All other opacity sources and electron donors are treated in LTE.

2.1. SEMI-EMPIRICAL ATMOSPHERE

To compare the physics in the dynamical simulation with the conclusions we would draw from a classical analysis of the time-average of the simulation, we analyze the dynamical simulation in a way similar to the construction of the VAL3 models. The time averaged intensity as a function of wavelength from the simulation is taken as the quantity to be reproduced by a semi-empirical model atmosphere. For an assumed temperature structure the equations of hydrostatic equilibrium, statistical equilibrium and radiative transfer are solved and the computed intensities are compared with the time average from the dynamical atmosphere. The difference is fed into an automatic scheme (Skartlien, 1994) that calculates the adjustment to be made to the semi-empirical temperature structure and the process is iterated to convergence.

This optimization problem is rather ill conditioned due to the width of the intensity contribution functions; any change on a scale substantially smaller than this width will not change the outgoing intensity. For this reason a smoothness criterion has been imposed on the semi-empirical temperature; above the classical temperature minimum the difference between a radiative equilibrium temperature structure and the semi-empirical temperature structure is described with a fifth order polynomial. Another reason for the ill-conditioned optimization problem is the fact that some height ranges are not represented with radiation formed there; in particular this is true for the heights between the formation heights of the Lyman continuum and the carbon continuum.

The atoms treated in non-LTE are the same as when calculating the time average of the intensity from the dynamic simulation: hydrogen, carbon, silicon, magnesium and aluminum.

Short-ward of infrared and mm wavelengths only in the UV are continua formed above the position of the temperature minimum in the VAL models. The semi-empirical temperature structure is thus determined by the time averaged intensities in the UV from 1500 Å (formed around the VAL temperature minimum) to the Lyman continuum (formed in the upper chromosphere in the VAL models).

The final semi-empirical temperature structure is typically able to reproduce the time averaged intensity to within 20 K in radiation temperature above 100 nm and to within 100 K in the Lyman continuum below 91.2 nm.

3. Results

3.1. FORMATION OF CONTINUUM RADIATION

Our inferences about the solar chromosphere are based on our analysis of the light we receive. To properly interpret our observations we need to know how that light is produced. In this section we discuss the formation of the continuum radiation at four wavelengths (the dominant bound-free opacity source given in parenthesis): 207nm (Al I), 152nm (Si I), 110nm (C I) and 91.2nm (Lyman continuum). The intensities discussed below are for the wavelength just short-ward of the respective bound-free opacity edge. These continua span a range of heights of formation and ionization potentials. We will see that concepts that work well in the static photosphere do not necessarily work in the dynamic chromosphere.

The contribution to the emergent intensity from a location $(z, z + dz)$ can be written

$$\delta I_\nu = [S_\nu][\exp(-\tau_\nu)][\sigma_\nu][ndz] , \quad (3)$$

a product of the source function, an attenuation factor, the cross-section and the column density of emitting atoms.

The source function is more or less strongly coupled to the Planck function which is very temperature sensitive in the UV, varying as $\exp(-\text{const}/T)$, but varies linearly with temperature in the mm wavelength range.

In a dynamic atmosphere, with shocks present, the contribution function for the intensity may be bimodal, with one peak around $\tau_\nu = 1$ and another at a shock at smaller optical depth. The shock may make a large contribution to the intensity because the source function can become extremely large and outway the small number density of emitting atoms at small optical depth. This is especially true at short wavelengths where the shock temperature increase gives an exponential increase in the Planck function. In this case the mean height of formation may well be somewhere between the shock and optical depth one and have no relation to either formation region. With this in mind we now consider the detailed behavior of the Al I, Si I C I and H I continua.

Figures 2–3 show the formation of the continuum intensities in the four continua at two different times in the dynamical simulation. The temperature is shown together with the source function, the contribution function to the intensity, the radiation temperature of the emergent intensity and the height and monochromatic optical depth scales.

Figure 4 gives the evolution in time over a short part of the full dynamic simulation of 7500 seconds.

The Al I continuum with its edge at 207 nm is formed deep, around $\lg \tau_{500} = -0.66$ at a height of 92 km. The mean depth of formation is below $\tau_\nu = 1$ because the contribution function gives more weight to larger depths due to the outward temperature drop. Aluminum has a low ionization potential, so it is nearly all ionized and Al I is not the main ionization stage. This makes the opacity very temperature

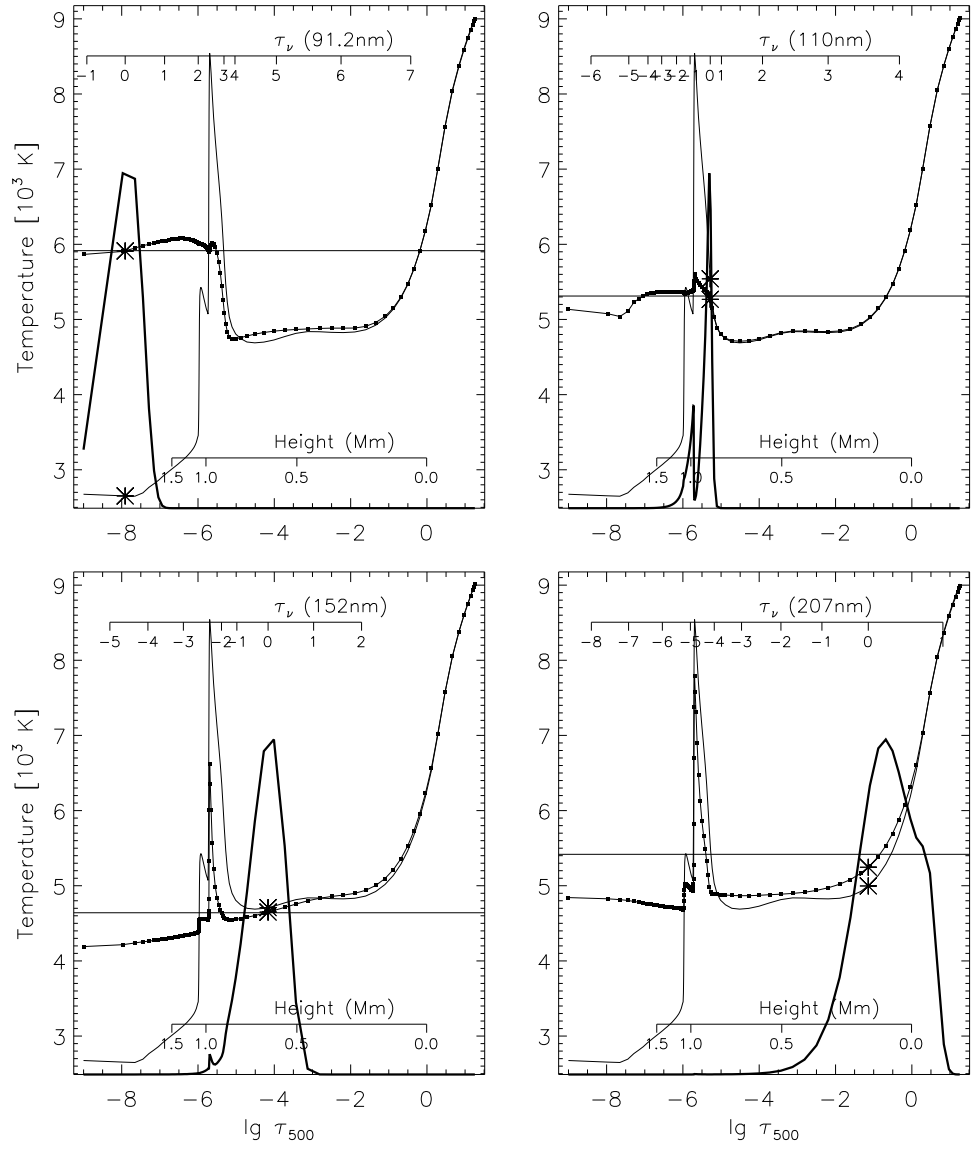


Fig. 2. Snapshot from the dynamical simulation at $t=1530$ s. Temperature (thin solid line, same in all four panels), source function (dotted) and the contribution function to the intensity (thick solid) as functions of $\lg \tau_{500}$. The temperature and the source function at $\tau_\nu = 1$ are marked with asterisks. The radiation temperature of the outgoing intensity is shown as a horizontal line. Four different wavelengths are shown corresponding to the Lyman continuum at 91.2 nm (top left panel), C I continuum at 110 nm (top right), Si I continuum at 152 nm (bottom left) and the Al I continuum at 207 nm (bottom right).

sensitive. The source function is slightly larger than the Planck function due to the non-LTE over-ionization. The source function at $\tau_\nu = 1$ is thus above the Planck function at that point and the emergent intensity is even higher due to the mean

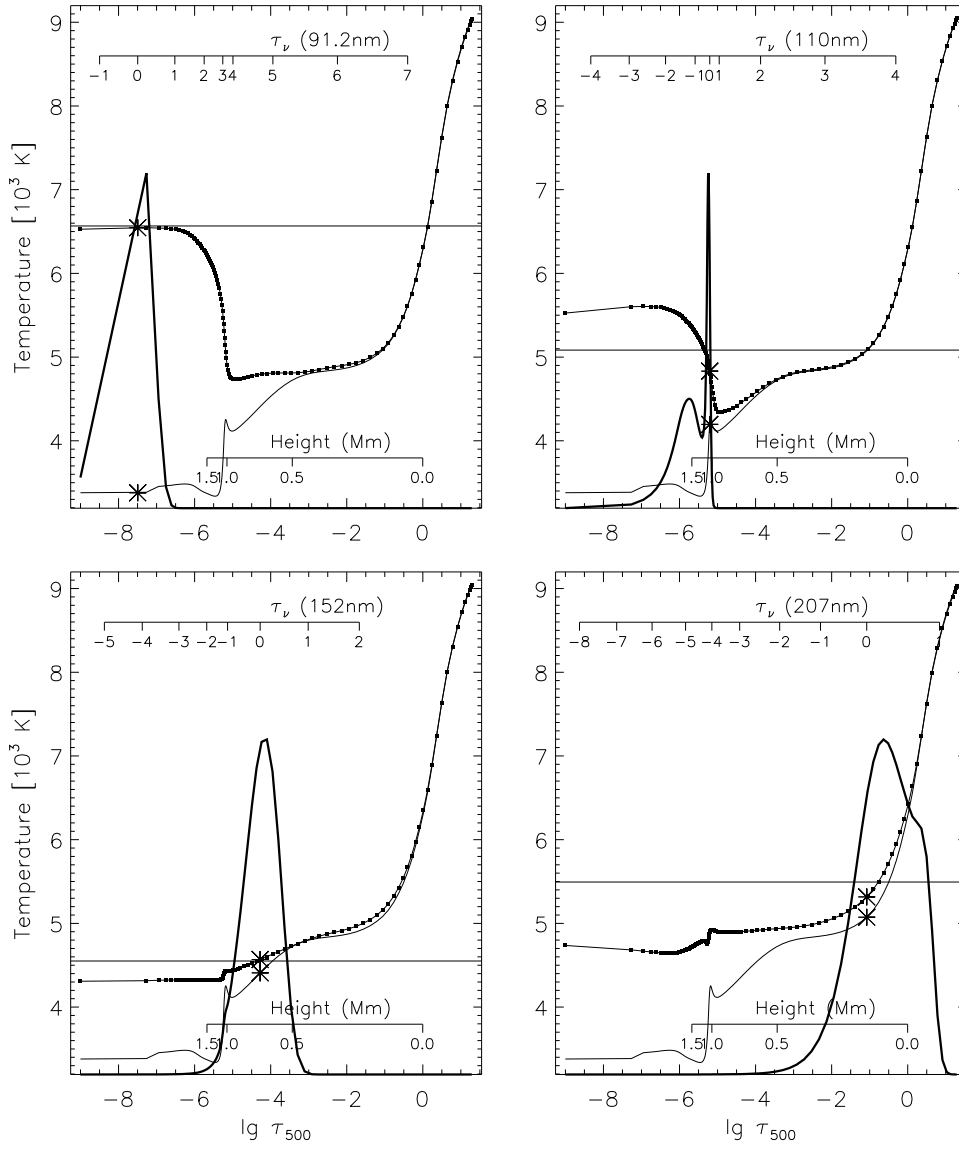


Fig. 3. As Fig. 2 but at $t=1610$ s.

formation depth being below $\tau_{\nu}=1$. These effects do not vary much in time and the emergent intensity, the source function and the Planck-function thus vary in phase (Fig. 4). However, because of the temperature sensitivity of the ionization stage and hence opacity, an increase in temperature produces further ionization, which leads to a smaller opacity, so one sees in deeper to yet higher temperature. Thus the variation in radiation temperature will be larger than the variations in gas temperature at the mean formation height; the rms of the radiation temperature in the simulation is

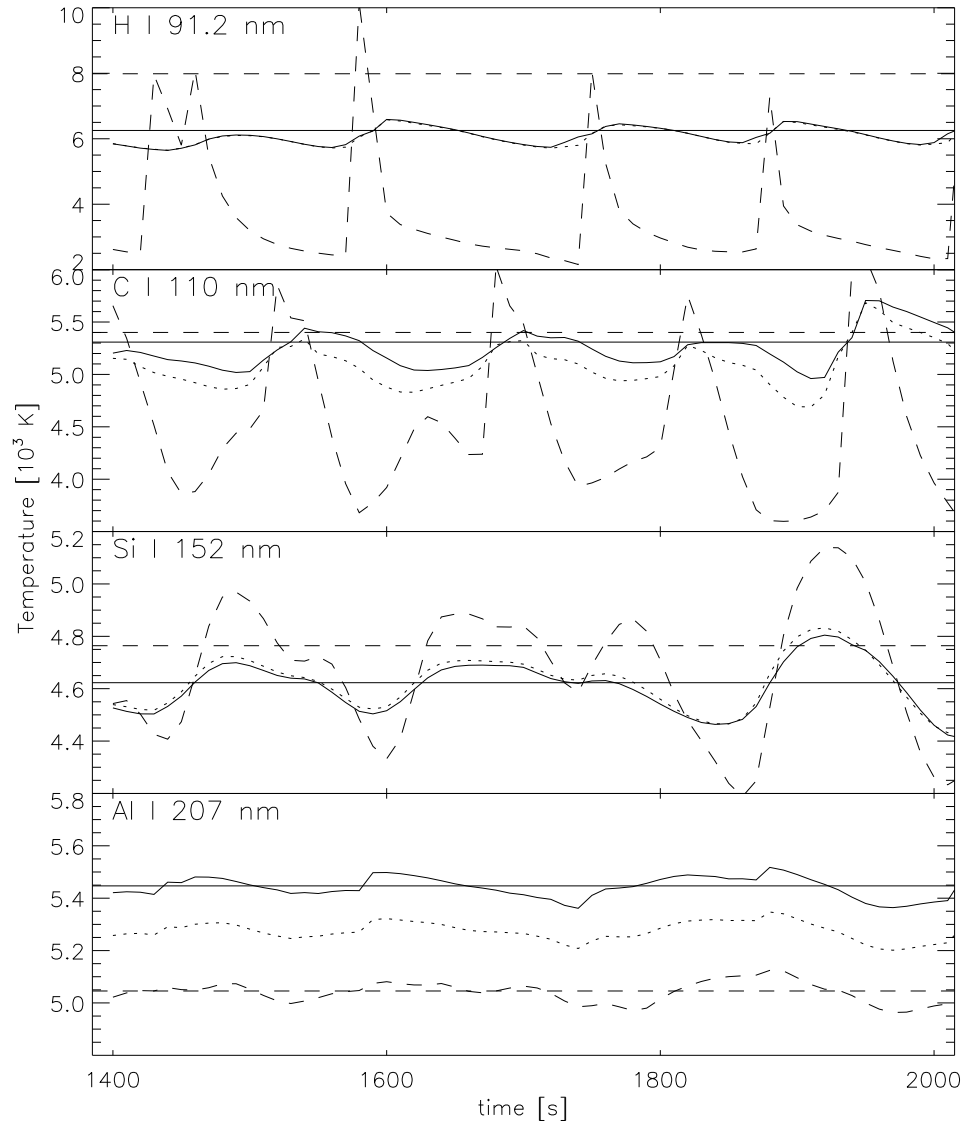


Fig. 4. The radiation temperature of the outgoing intensity (solid), the source function at $\tau_\nu = 1$ (dotted) and the temperature at $\tau_\nu = 1$ (dashed) as functions of time for a small part of the dynamical simulation for four wavelengths. The horizontal lines show the radiation temperature of the mean of the outgoing intensity (solid) and of the mean of the Planck function (dashed) with the mean taken over this part of the simulation. The means from the complete simulation will be slightly different. The non-linear averaging is clearly shown with the radiation temperature of the intensity mean being close to the maximum intensity and likewise for the Planck function. The source function varies much less than the Planck function due to the non-LTE decoupling. The radiation temperature of the outgoing intensity does not show the shock signature of a discontinuous rise for the same reason.

40K while the rms of the gas temperature at a *fixed* height of 100km is 17K. The rms variation in mean formation height is 0.04 in $\lg \tau_{500}$ corresponding to 7 km.

The silicon continuum at 152 nm is formed around $\lg \tau_{500} = -4.3$ at a height of 648 km. The rms variation in the mean height of formation is 0.11 in $\lg \tau_{500}$ corresponding to 49 km. Silicon has a moderate ionization potential. Hence, near the formation depth, silicon is $\approx 80\%$ ionized. Due to the lower temperatures in the dynamic model, compared with a classical model with a chromosphere, and the temperature sensitivity of the silicon ionization, the formation height is substantially higher than in a semi-empirical model. The source function and Planck function are nearly uniform in the formation region, because it is below the region where shocks significantly modify the temperature structure (and hence the source function) and above the region of decreasing photospheric temperatures. This layer is near the region where shocks create an instantaneous temperature increase as they pass through. The intensity is produced close to $\tau_\nu = 1$ (4), and the classical contribution function there dominates the intensity formation. There may be a secondary peak in the contribution function at a shock at smaller optical depth, but such secondary maxima always make smaller contributions to intensity. As a result, fluctuations in the radiation temperature follow the thermal temperature at $\tau_\nu = 1$. However, the radiation temperature fluctuations have a smaller amplitude (rms of 86 K) than those in the gas temperature (rms of 210 K) due to the decoupling of the non-LTE source function and the Planck function.

The carbon continuum at 110 nm is formed at $\lg \tau_{500} = -5.6$, just below where shocks become strong. The rms variation in the mean height of formation is 0.32 in $\lg \tau_{500}$ corresponding to 168 km. Carbon has a high ionization potential, so is nearly all neutral there. Since this is near the level of strong shock formation, the source function responds to both the high temperatures at the shock and the low temperatures in their wake. However, the source function varies much less than the Planck function, because it is controlled by radiation, not by collisions. The intensity contribution function is often bi-modal, with one peak near $\tau_\nu = 1$ and the other at the shock (Figs. 2–3). The radiation temperature is generally above the gas temperature at $\tau_\nu = 1$ and does not dip as low. Only when a strong shock is formed by merging of shocks at small heights does the temperature in the wake fall low enough to make the source function follow. The radiation temperature of the emergent intensity shows a large rms variation of 165 K. The gas temperature at $\tau_\nu = 1$ shows an rms variation of 636 K.

The Lyman continuum at 91.2 nm is formed close to the top of the computational domain. The monochromatic optical depth at the top boundary is around 0.1 and the emergent intensities will be affected by the treatment of the matter leaving the computational domain and by the absence of a magnetic canopy in the simulations (see Section 4). Keeping this in mind, the continuum radiation is formed around $\lg \tau_{500} = -8$ with an rms variation of 0.27 in $\lg \tau_{500}$ corresponding to 59 km in height. The source function is almost completely decoupled from the Planck function; this gives a much smaller variation in the radiation temperature of the emergent intensity (rms of 256 K) than in the gas temperature at $\tau_\nu = 1$ (rms of 1910 K). The gas temperature shows a rapid almost discontinuous rise when the shocks pass while the radiation temperature shows no such shock signature due to the decoupling of

the source function from the Planck function. The timescale for hydrogen ionization/recombination is long at the height of formation of the Lyman continuum. The recombination then takes place behind the shocks leading to a maximum radiation temperature after the maximum gas temperature at $\tau_\nu = 1$.

Continua formed in the photosphere, e.g. Al I with the edge at 207 nm, and up to about 0.5 Mm, e.g. Si I with the edge at 152 nm, thus have contribution functions peaked near $\tau_\nu = 1$ and have no secondary maxima at the height where shocks exist because the number of their atoms at that height is extremely small. The C I continuum with the edge at 110 nm is formed close to where shocks form and often exhibits a bimodal contribution function (Figs. 2–3). Even though the number of atoms at shock forming heights is small, the exponential temperature sensitivity of the Planck function outweighs this factor.

Above the photosphere, the source function is so decoupled from the Planck function that variations in intensity can *not* be taken as a proxy for gas temperature variations (Fig. 4). Even in the photosphere such a one-to-one correspondence between intensity variation and gas temperature variation is not possible because of the dependency of the formation height on the opacity and therefore on the temperature.

3.2. SEMI-EMPIRICAL ATMOSPHERE

Figure 5 shows the time average of the temperature as a function of height in the dynamical simulation as a thick solid line. This average dynamic temperature structure shows no chromospheric rise. The corresponding semi-empirical temperature structure (dashed) is obtained by treating the temperature as a function of height as a free parameter and iterating to get the best possible fit between the intensities calculated from the semi-empirical model and the time average of the intensity as a function of wavelength calculated from the dynamical simulation (see Section 2.1). Also shown in the figure are the range of temperatures in the simulation (thin solid lines), the starting model for the dynamical simulation (dotted) and the semi-empirical model FALA constructed to reproduce the solar dark internetwork regions (dot-dashed) (Fontenla *et al.*, 1993).

The striking feature of Fig. 5 is that the time average of the temperature as a function of height in the dynamical simulation shows *no chromospheric temperature rise* while the best match semi-empirical model has a classical chromospheric temperature rise.

The temperature averaging in the dynamic simulation was done for given heights but the result is independent of the averaging procedure. The same monotonic temperature decrease with height is obtained by averaging on fixed column masses (Lagrangian grid). Averaging the thermal energy instead of the temperature again gives the same result.

Why is a semi-empirical temperature rise needed to reproduce the time-averaged intensities? Although the diagnostic continua were calculated in non-LTE as explained in Section 2.1, we will nevertheless start this discussion with a test case where all diagnostic continua were calculated in LTE.

In LTE one would expect the best match semi-empirical temperature to be close to the maximum temperature due to the exponential temperature sensitivity of the Planck function in the UV. This is not the case — the semi-empirical temperature

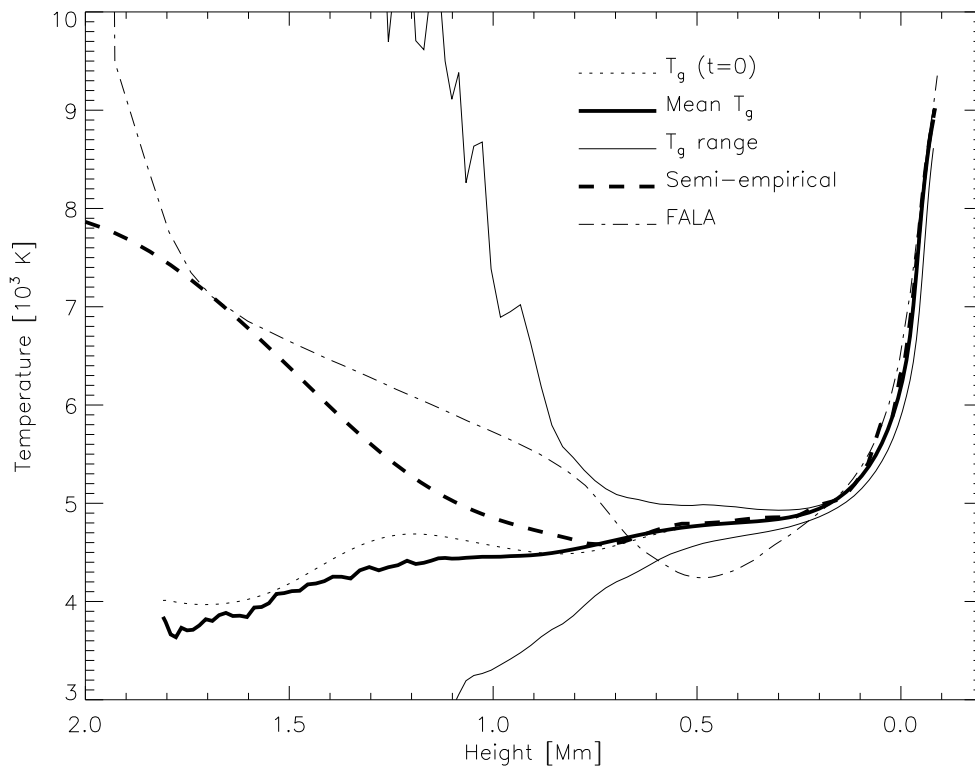


Fig. 5. Time average of the temperature in the dynamical simulation (thick solid), the range of temperatures in the simulation (thin solid), the semi-empirical model that gives the best fit to the time average of the intensity as a function of wavelength calculated from the dynamical simulation (thick dashed), the starting model for the dynamical simulation (dotted) and the semi-empirical model FALA (dot-dashed). The maximum temperatures are only reached in narrow shock spikes of short duration. The semi-empirical model giving the same intensities as the dynamical simulation shows a chromospheric temperature rise while the mean temperature in the simulation does not.

lies much lower than the maximum shock temperatures even in LTE. This is partly because the maximum temperatures occur in very narrow shock spikes of short duration and also because the width of the contribution function smears out the influence of the spikes on the intensities. The radiation temperature of the average intensity is above the average temperature, however, because of the exponential temperature dependency of the Planck-function. This results in a semi-empirical temperature rise.

In non-LTE the effects are much the same. The source function is partly decoupled from the Planck-function and shows much less variation with time (see Fig. 4). However, the non-linear weighting of the higher temperatures is similar to the LTE-case and one gets a semi-empirical temperature rise. The intensities thus vary less and have a different mean radiation temperature than in the LTE case. Despite these differences, the best fit semi-empirical temperature structure is very similar in LTE and non-LTE, even though the mean intensities are different.

The mechanisms operating in the Lyman continuum are different from the other continua due to the slow ionization/recombination rates. These effects have been neglected for the other continua since these model atoms were not included self-consistently in the dynamic calculation (see Section 4 for a discussion of possible consequences of this neglect). At a given time the viscous dissipation in the shocks together with the pressure work leads to a high temperature. This shock spike is very strong because the long timescales for hydrogen ionization/recombination prevents the energy from going into ionization energy (Carlsson and Stein, 1992). Hydrogen is ionized further back into the post-shock region lowering the temperature. Even further back, the recombination takes place releasing the energy in the form of radiative cooling. Integrated over time at a given height, the viscous dissipation is balanced by the radiative cooling and there is no increase in the thermal energy. There is, however, an increased radiation compared with the radiative equilibrium starting at atmosphere due to the radiative cooling. The slow hydrogen ionization/recombination thus increases the intensity and drastically lowers the amplitude of the intensity variations.

3.3. VELOCITY TRANSFER FUNCTION

The velocity spectrum as a function of frequency changes with height, both in amplitude and phase. The velocity amplitude of propagating waves increases with height in a stratified atmosphere to maintain a constant flux as the density decreases. Damping reduces this amplitude increase. Propagating modes also show a phase shift due to their finite phase speed. For evanescent modes one expects more damping but no change in phase as a function of height.

We describe the change in the velocity spectrum in the simulations with a transfer function, H_{z_1, z_2} , defined as

$$F[v_{z_2}] = H_{z_1, z_2} F[v_{z_1}], \quad (4)$$

where $F[v_{z_1}]$ denotes the Fourier transform of the velocity at height z_1 .

The transfer function is thus a complex valued function where the absolute value gives the ratio of velocity amplitude between the two heights and the phase gives the $(v_{z_2} - v_{z_1})$ phase difference.

Figure 6 shows the velocity transfer function over height intervals of 100 km as a function of height in the atmosphere. The large spread in phase and amplitude amplification in the bottom panels is due to low power at high frequencies at a height of -70 km. The phase difference plots show the expected behaviour with no phase difference in the evanescent regime below the cut-off frequency (which varies from 4 mHz at the bottom to 5 mHz at 300 km height, see Fig.1). The phase difference for propagating waves is what is expected from a phase speed asymptotically approaching the sound speed for high frequencies. The velocity amplitude in the evanescent regime is nearly constant with height indicating strong damping, since for undamped waves the amplification factor would be 1.3–1.7 over 100 km with a pressure scale height of 110–190 km. For higher frequencies, the amplification approaches the undamped value.

The transfer function from the height of the piston to the formation height of the Fe I line at $\lambda 396.68$ nm (about 260 km) was used to compute the piston velocity (see

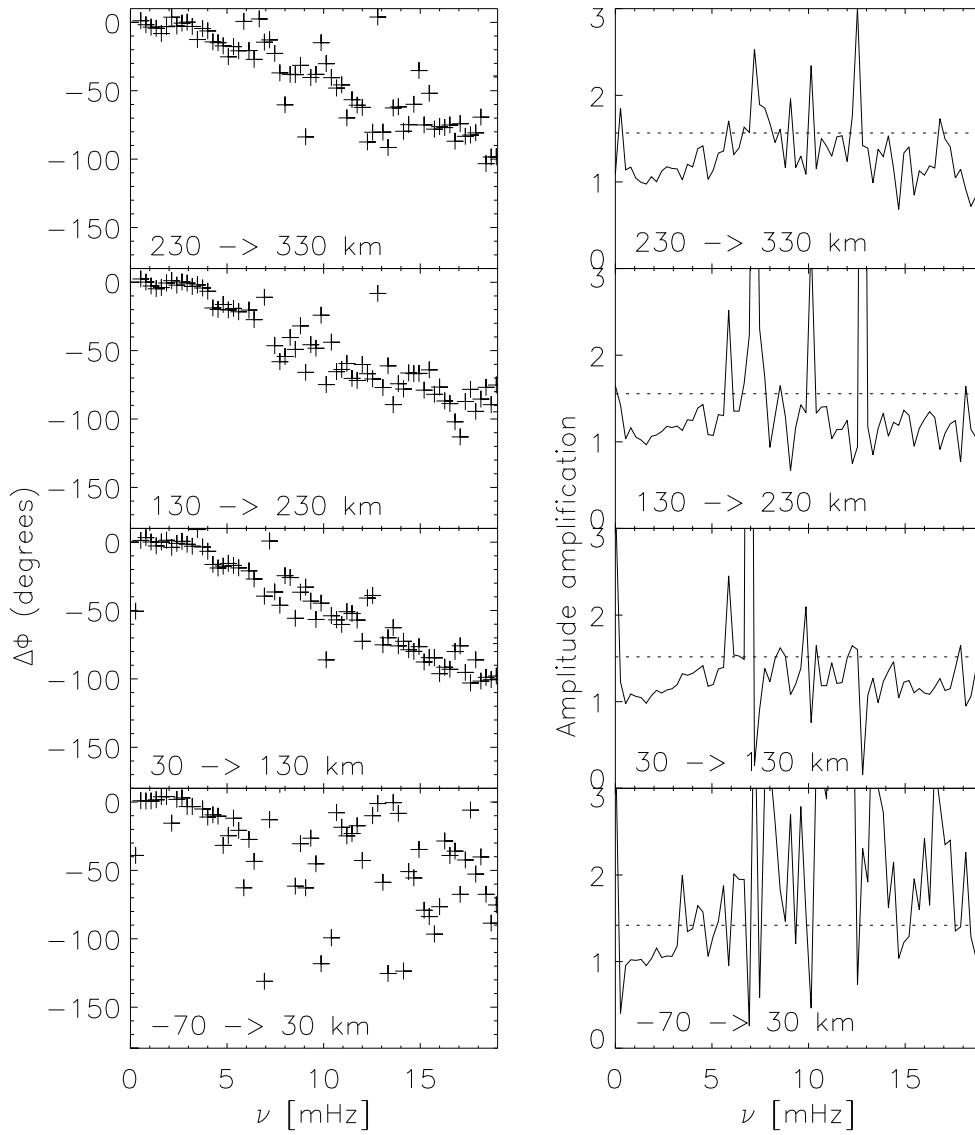


Fig. 6. Velocity transfer function over height intervals of 100 km. The large spread in phase and amplitude amplification in the bottom panels is due to low power at high frequencies at a height of -70 km. The dotted line in the right panel shows the undamped amplification factor $\exp(\Delta z/2H)$.

section 2). Provided the transfer function is independent of the piston velocities, this procedure should recover the Fe I Doppler shifts as the velocity at the height 260 km in the model. The transfer function from two different velocity fields is shown in Fig. 7 together with the observed Doppler shifts and the velocities in the simulations at the height 260 km. The transfer functions for the two different velocity fields are rather similar at low frequencies. At high frequencies there is a lot of noise due to

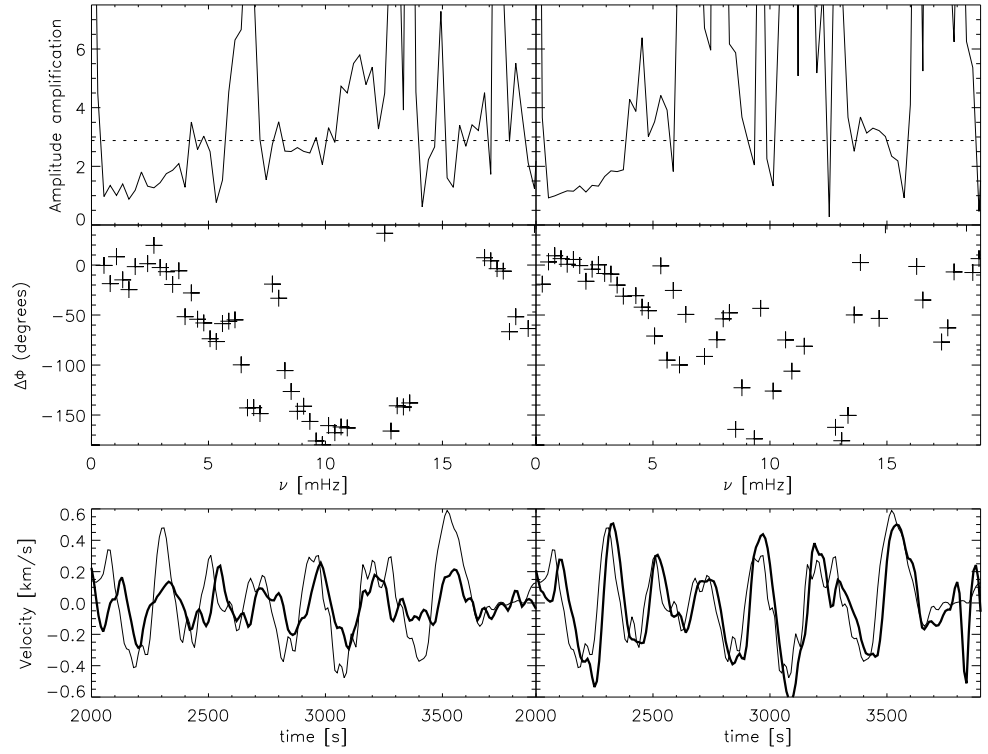


Fig. 7. Velocity transfer function from the height of the piston to the formation height of the observed FeI line at $\lambda 396.68$ nm (about 260 km) with velocity amplification in the top panels (dotted line: undamped amplification factor of $\exp \Delta z / 2H$), phase shift in the middle panels and the velocity at a height of 260 km in the simulation (thick) compared with the observed Doppler shift in the FeI line (thin). The left hand panels show the results from a piston velocity taken to be the observed FeI Doppler shifts scaled by 0.2. The right hand panels show the results from a piston velocity calculated with the help of the transfer function of the left panel. The observed Doppler shifts are quite well recovered except for a remaining phase shift of about 22 seconds.

the small power at those frequencies at the height of the piston. The piston velocities used for the computations shown in the left hand panels contain more high frequency power and less low frequency power than the piston velocities for the computations shown in the right hand panels. This is clearly visible in the amount of noise in the transfer function.

Just scaling the observed Doppler shifts with a factor of 0.2 gives too little power in the evanescent regime. Using this transfer function to adjust the piston velocities gives a good recovery of the Doppler shifts (Fig. 7, lower panels). Note, however, that the computed velocities lag the observed Doppler shifts by about 22 seconds.

The velocity amplitude at 260 km height is about 10% of the local sound speed. Higher up in the atmosphere we would expect the concept of a transfer function as a property of the atmosphere to break down because the large amplitude perturbations modify the atmosphere significantly.

3.4. FORMATION OF H_{2V} BRIGHT GRAINS

The quasi-periodic emission in the core of the H and K lines of ionized calcium is asymmetric with often strong emission on the violet side of the line center (so called H_{2V} and K_{2V} bright grains) and seldom any emission on the red side. This asymmetry is explained by the correlation between velocity and temperature. We will here go further, in an attempt to clarify what factors influence the separation of the H_2 peaks and where they are formed. We will also analyze different simulations and show that the occurrence of grains is determined wholly by the velocity field and *not* by the previous history of the atmosphere. Finally, we will reveal the characteristics of the photospheric velocity field that are sufficient to create bright grains. In the simulations we will show results for the H-line in order to be able to compare with observations of that line.

3.4.1. *Formation of emergent H-line intensity*

The emergent intensity is given by the formal solution of the transfer equation:

$$I_\nu = \int_0^\infty S_\nu e^{-\tau_\nu} d\tau_\nu. \quad (5)$$

The intensity contribution function can thus be split into the source function, S_ν , an exponential attenuation factor ($e^{-\tau_\nu}$) and the product of the cross-section and the column density of emitters ($d\tau_\nu$). This formal solution can be rewritten as:

$$I_\nu = \int_{z_0}^{z_1} S_\nu \tau_\nu e^{-\tau_\nu} \frac{d \ln \tau_\nu}{dz} dz. \quad (6)$$

Now the integration variable is geometrical height, z , and the optical depth factors have been reorganized as: $\tau_\nu e^{-\tau_\nu}$ which has a sharp peak at $\tau_\nu = 1$ and $d \ln \tau_\nu / dz \equiv \chi_\nu / \tau_\nu$, where χ_ν is the monochromatic opacity per volume and thus a measure of the density of emitting particles. This last factor is thus important when there are many emitting particles (large χ_ν) at small optical depth (small τ_ν), a situation that typically arises in the presence of strong velocity gradients. It is this factor that is responsible for the asymmetry of the CaII lines.

In the following series of figures (Figs. 8–12) the formation of the H_{2V} bright grains is shown in the form of the contribution function to intensity and the factors entering its calculation. The figures all have four panels with the full contribution function in the lower right panel and the three factors above in the three other panels. The functions are shown as grey-scale images as functions of frequency in the line (given as Doppler shift) and height in the atmosphere. The image in the lower right panel is thus the product of the three other images. All panels also show the velocity as a function of height with upward velocity positive (to the left in the figure) and the height where $\tau_\nu = 1$ (grey line). The top right panel also shows the Planck function (dotted) and the source function (dashed) with high values to the left. In the bottom right panel the emergent intensity is also shown as a function of frequency. The time in seconds from the start of the simulation is shown in the top left panel.

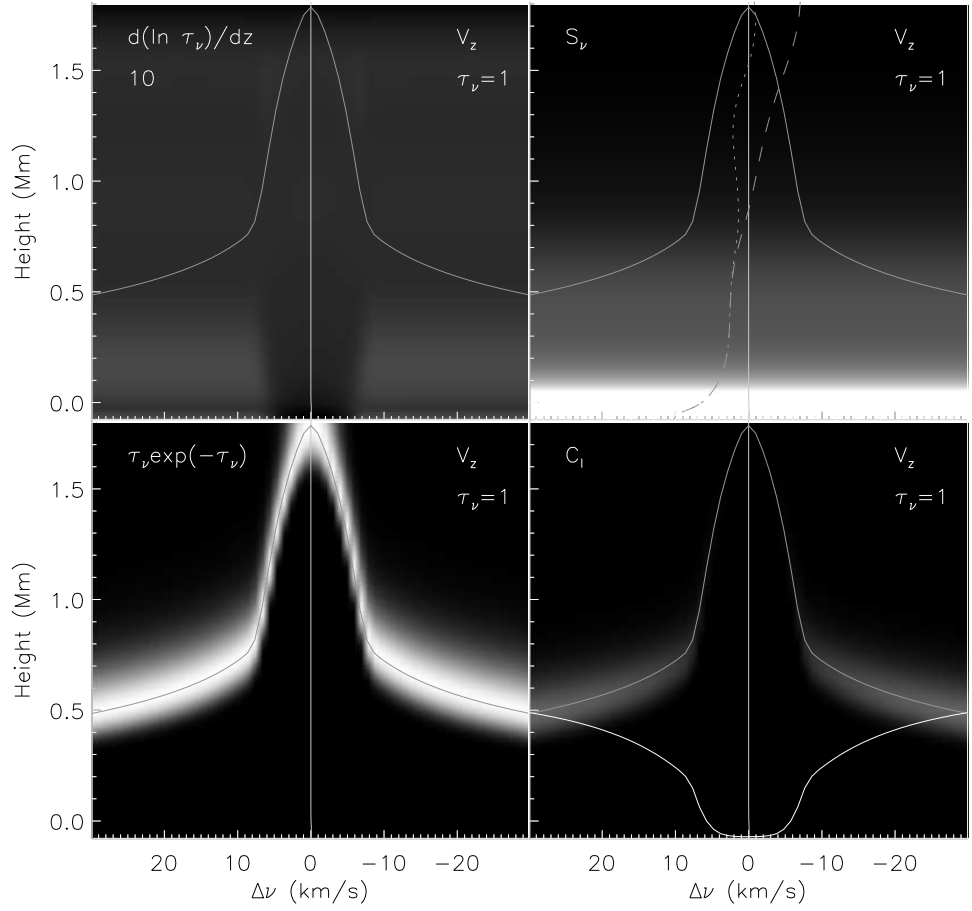


Fig. 8. The formation of the H_2V bright grains is shown in the form of the contribution function to intensity (lower right) and the factors entering its calculation, $d \ln \tau_\nu / dz$ (upper left), S_ν (upper right) and $\tau_\nu \exp(-\tau_\nu)$ (lower left). The functions are shown as grey-scale images as functions of frequency in the line (given as Doppler shift) and height in the atmosphere. In all panels are also shown the velocity as a function of height with upward velocity positive (to the left in the figure) and the height where $\tau_\nu = 1$ (grey line). In the top right panel is also shown the Planck function (dotted) and the source function (dashed) with high values to the left. In the bottom right panel the emergent intensity is also shown as a function of frequency. The time in seconds from the start of the simulation is shown in the top left panel.

Figure 8 shows the situation at the start of the simulation before any waves have traveled through the atmosphere. The atmosphere is static and the velocity is zero everywhere. The emergent intensity (lower right panel) shows no emission and all factors entering the calculation of the contribution function are symmetric with respect to line center.

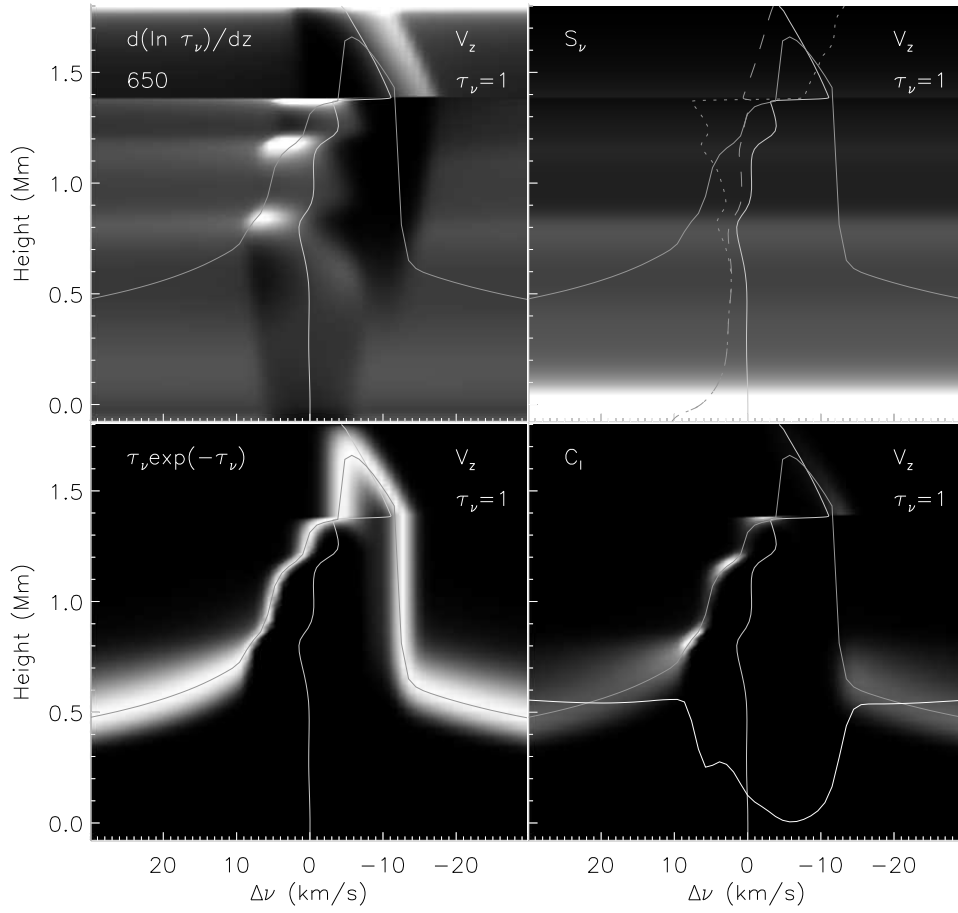


Fig. 9. As Fig. 8 but for $t=650$ s.

Figure 9 shows the situation after 650 seconds. Several shocks have traveled through, there is one at 1.4 Mm and two waves behind that shock that are steepening. The source function is constant across the line at a given height, (image, upper right panel) because of the assumption of CRD, but is substantially below the Planck function due to the non-LTE decoupling (compare dotted and dashed lines, upper right panel). The $\tau_\nu e^{-\tau_\nu}$ factor gives weight around $\tau_\nu = 1$ (lower left panel). The $d \ln \tau_\nu / dz$ factor gives weight to those depths where we have a velocity gradient such that we have large opacity at a given frequency but a small optical depth (upper left panel). The strongest combined effect is seen where the source function is also large at 0.8 Mm. The absence of a red peak where $\tau_\nu=1$ on the red side (at -12 km/s) is due to the lack of opacity there since the atomic absorption profile has been shifted to the blue.

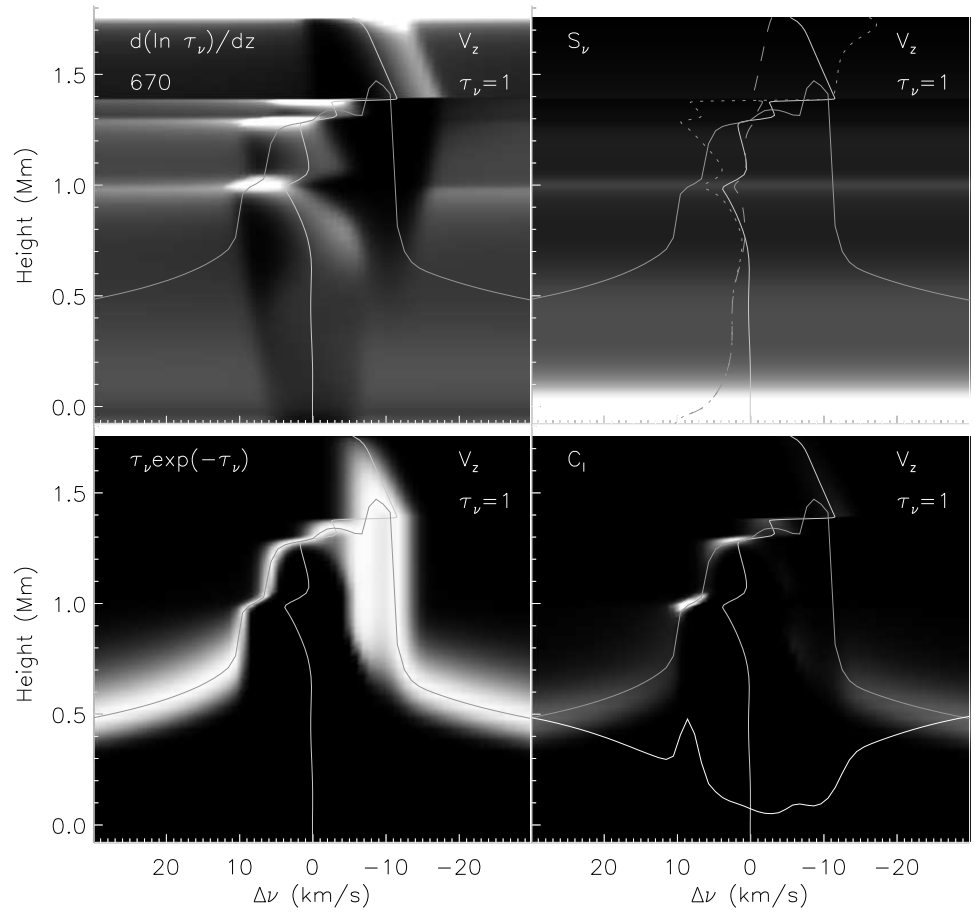


Fig. 10. As Fig. 8 but for $t=670$ s.

Figure 10 shows the situation 20 seconds later. The upper wave has become a shock and is about to merge with the top shock. Due to the non-LTE decoupling, the source function does not show an extreme maximum at that height and the dominant maximum in the contribution function is from the wave at 1 Mm that has not quite shocked yet. There is a corresponding peak in the emergent intensity profile. The maxima in the upper left panel occurs where we have large velocity gradients, not at the center of the atomic absorption profile but close to $\tau_\nu=1$. The distance from line center for the bright emission is thus set by the velocity in the immediate post shock material plus an absorption profile width that is sensitive to the microturbulence.

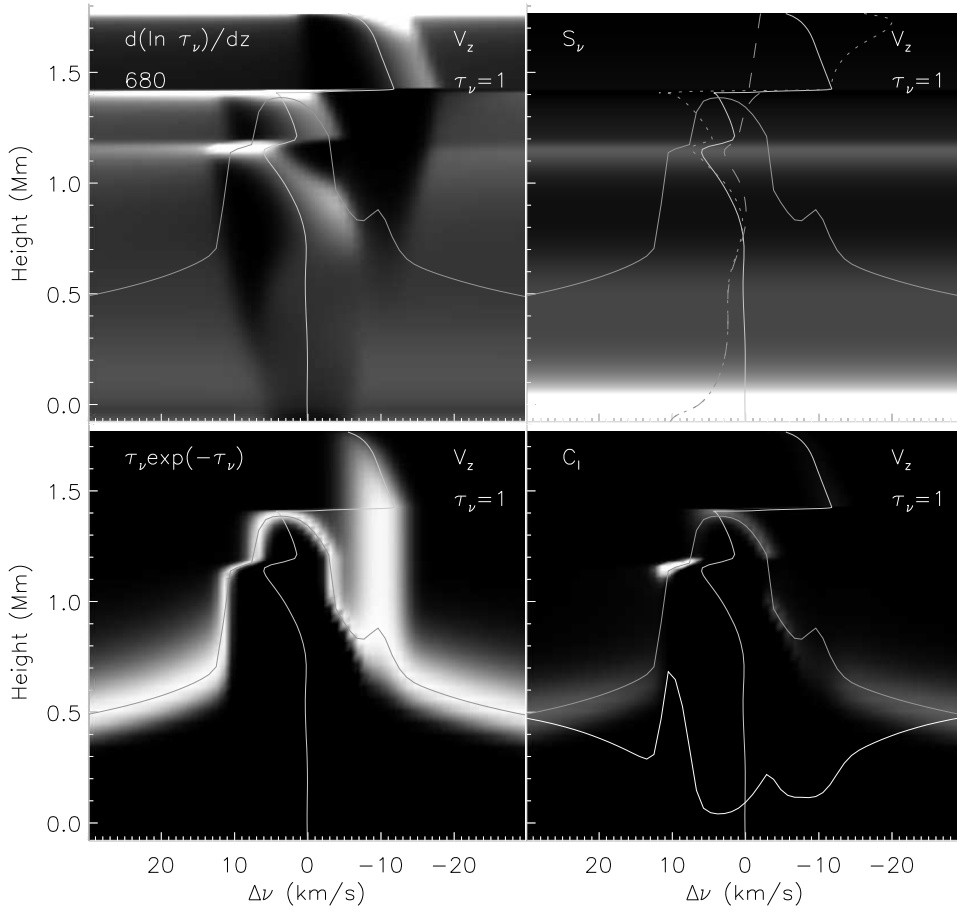


Fig. 11. As Fig. 8 but for $t=680s$.

Figure 11 shows the situation 10 seconds later. The two top shocks have now merged into one and the wave behind is steepening into a shock. The H_2V emission comes from 1.2 Mm where the source function has a maximum. The top shock is above the height where $\tau_\nu=1$ at line center and does not give any emission. There is some emission coming from the line center region where $\tau_\nu=1$ and there is still substantial emitting matter (top left panel). This emission gives rise to a line core emission peak that with time moves from blue towards red. This is a pattern often found in the simulations that is not clear in the observations.

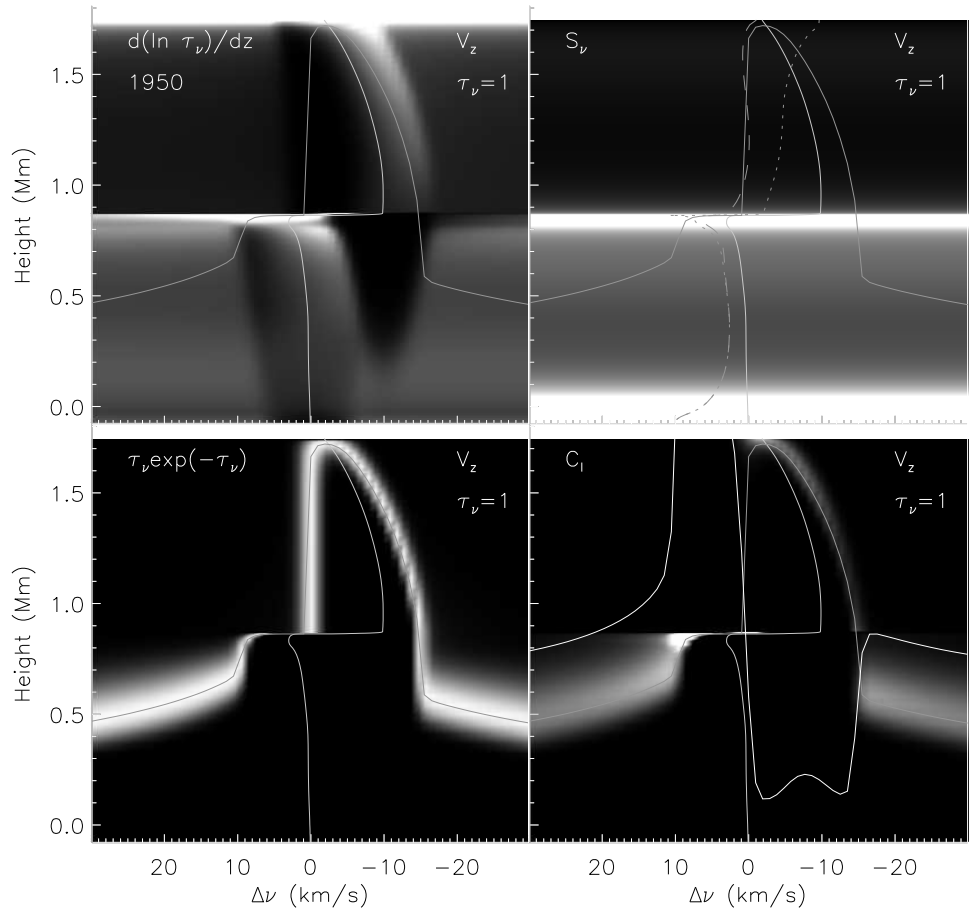


Fig. 12. As Fig. 8 but for $t=1950$ s. This is the time of the brightest grain.

Figure 12 shows the situation 1950 seconds from the start of the simulation when we have the strongest grain in the simulation. The wake of an earlier strong shock, produced by the merging of several shocks, has created a strong downfall into which another strong shock, resulting from new shock merging, propagates. This creates a strong shock at a low height of 0.87 Mm which produces a large source function as well as a large τ_ν gradient which gives rise to a very strong emission.

To get an asymmetric profile with no red peak thus requires a large velocity gradient at a small enough height that significant numbers of atoms are present. The position of the violet peak is set by the amplitude of the shock plus the width of the absorption profile. The brightness of the peak is set by the shock formation height with lower height corresponding to a brighter peak.

3.4.2. Comparison with observations

The piston velocities were chosen to reproduce the measured Doppler shifts in the iron line at 396.68 nm at a given slit position in the observations by Lites *et al.*, 1993. It is then natural to compare the computed behaviour of the H line with these observations. This is done in Fig. 13. The observations are not reproduced in all details but there is a general correspondence down to the level of individual grains. One may identify wing brightenings, periods of weak grains (*e.g.* $t=900\text{--}1450\text{s}$) and strong bright grains ($t=1450\text{--}2600\text{s}$).

The general agreement gives some confidence that the simulations describe the physical processes most important for the bright grain phenomenon. What are the important *discrepancies* between the simulations and the observations and what can be learnt from them? The simulations show a much larger contrast with a sharp transition to a very dark, rather flat core region. There are more details in the core region with frequent secondary maxima. Some of this discrepancy could be due to observational effects. Limited instrument resolution will cause a smearing in the wavelength domain. Scattered light both in the instrument and by the Earth's atmosphere will decrease the contrast and mix in a signal from other spatial positions on the sun. Seeing will also contribute to the total point spread function and in addition introduce a signal from more distant spatial points through image motion.

It is almost impossible to remove these effects from the observations since the various convolutions are poorly known. An additional difficulty with including these effects in 1-D simulations is the unknown spatial correlation. In lieu of a detailed study we just illustrate the effects to be expected by showing the simulation with various degrees of smearing in Fig. 14. Spatial smearing has been simulated by a smearing in the time domain. It is clear that the difference in the form of the profile and in contrast may be entirely due to observational effects. To obtain the maximum information content in the observations one thus has to spend a lot of effort on minimizing scattered light and effects of smearing by seeing.

A more robust difference with observations seems to be a difference in the time when the grains appear. It is possible to make an identification between observed grains and the grains in the simulations but it seems the grains in the simulations appear somewhat later in time (roughly 30 seconds). Note, however, that the piston velocities do not exactly reproduce the Doppler shifts in the iron line; there is a phase difference of 22 seconds. Ideally, the piston velocities should be modified until the iron line observations are matched exactly. To first order that would mean a shift by 22 seconds which would almost remove the discrepancy in the time of the grains.

3.4.3. Formation of the grain pattern

When do we get grains and when will there be no grains? We investigate the importance of the piston velocity pattern versus the previous history of the atmosphere by performing a simulation with a 3750 second piston velocity repeated twice. The piston velocity at $t=3750+t_0$ is thus identical to the piston velocity at $t=t_0$. The resulting H-profile as a function of time is shown in Fig. 15. The time evolution has been split into two panels with the right panel showing the second half of the simulation. The piston velocity is thus the same at the same vertical position in

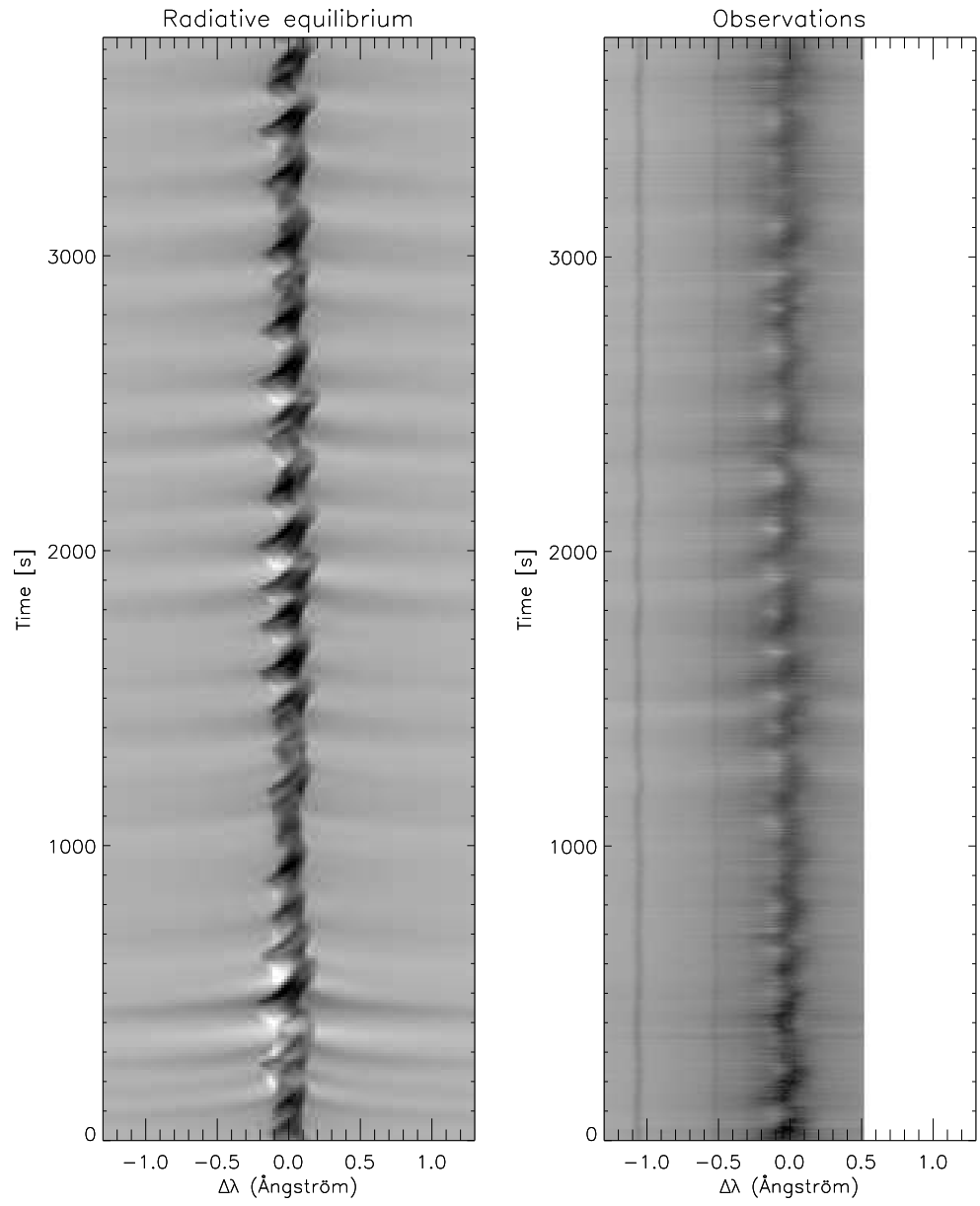


Fig. 13. The computed Ca II H line intensity as a function of wavelength and time compared with observations.

the two panels. It takes some time to set up the typical wave pattern which is the reason why there is little development with time in the beginning. The beginning of the second half of the simulation is also atypical since there is a sudden phase jump when the velocity pattern is repeated. This is also visible in a comparison

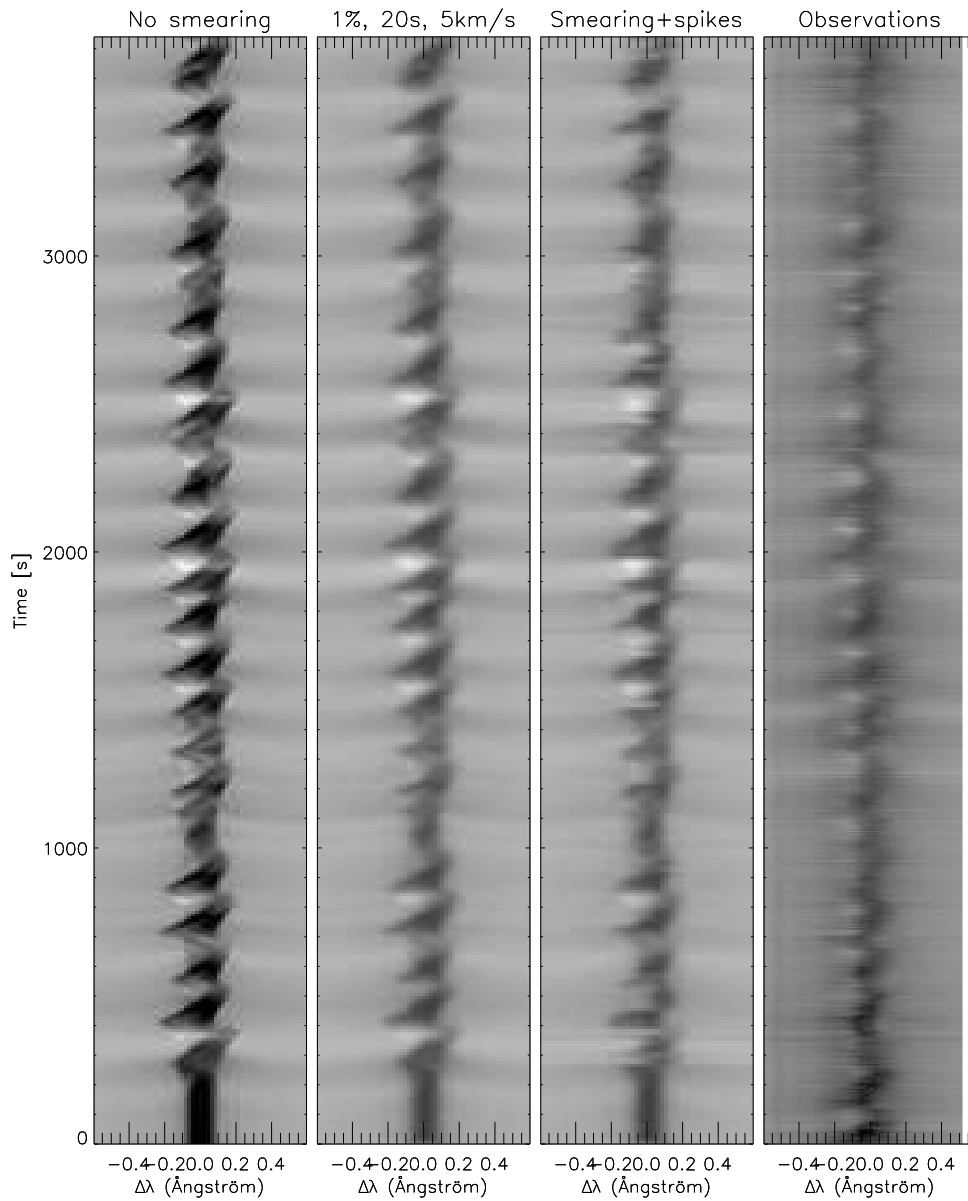


Fig. 14. The computed Ca II H line intensity as a function of wavelength and time compared with observations. The leftmost panel shows the unsmearred results from the simulation. In the second panel the simulation has been convolved with a Gaussian point spread function with FWHM of 20 seconds in the time domain and 0.066 Å (corresponding to 5 km/s) in the wavelength domain. Scattered light amounting to 1% of the continuum intensity has been added. In the third panel image motion has been simulated by shifting the sequence in time with a random function. The same smearing and scattered light as in the second panel was also added.

between the computed velocity at 260 km and the Doppler shift of the iron line: the beginning of the second half of the simulation shows a poor match. Outside these startup periods, the two halves of the simulation show almost exactly the same grain development with no pronounced grains in the time intervals 900–1450s and 4650–5200s and strong grains in the time intervals 1450–2600s and 5200–6350s. We conclude that there is no long time memory in the atmosphere and that the bright grain pattern is completely determined by the velocity pattern.

What in the velocity field is triggering the formation of bright grains? Explanations in the literature go from very high frequency waves (period on the order of 30s) through the process of shock overtaking (Rammacher and Ulmschneider, 1992), three minute waves (Carlsson and Stein, 1992) to five minute oscillations (Kalkofen *et al.*, 1992). To study the importance of propagating frequencies versus evanescent frequencies we have performed two additional simulations where the piston velocities of the full simulation have been either low-pass or high-pass filtered relative to the cut-off frequency at the location of the piston (4.5 mHz). The comparison with the full simulation is shown in Fig. 16. The simulation with only high frequencies in the piston velocities is almost identical to the full simulation after 1600s. In the beginning of the time sequence there is very much increased grain activity. This is due to wave overtaking in the unperturbed atmosphere caused by a few strong spikes in the piston velocity field similar to excitation by velocity impulses (Kalkofen *et al.*, 1992). During the period $t=1000$ –1450s the high frequency simulation shows more pronounced grains than in the full simulation, the low frequencies modulate the behaviour of the high frequency waves. In the period of the most pronounced grains, $t=1450$ –2600s, the high frequency simulation shows almost identical behaviour to the full simulation. The low frequency simulation show no grains after the first phase. We conclude that the propagating frequencies are most important for the formation of grains but lower frequency components in the photospheric velocity field modulate the behaviour.

From the analysis of contribution functions (Section 3.4.1) one would expect strong grains to be correlated with large velocity amplitudes around a height of 1Mm. This is clearly shown in Fig. 17 where the velocity as a function of time is shown for eight different heights in the atmosphere. The strong grain at $t=1950$ s is furthermore shown to be caused by a low shock-formation height (discontinuous rise of the velocity) due to the wave propagating into a region of downfall from previous waves. It is possible to trace back the strong perturbations down to photospheric heights but the picture is not altogether simple. Waves of different frequencies propagate at different phase speeds; at the cut-off frequency the phase speed is infinite and the waves line up vertically, at high frequencies the phase speed approaches the sound speed. These different phase speeds at different frequencies can be seen in the figure as high frequency perturbations appearing at progressively later times with respect to lower frequencies. The interference of these different modes produces the velocity pattern at any given height. When we reach shock forming heights the pattern changes with the whole shock propagating at a supersonic speed. Since the shocks may propagate with different speeds we may get shock overtaking but in general this takes place at heights above the formation height of the grains.

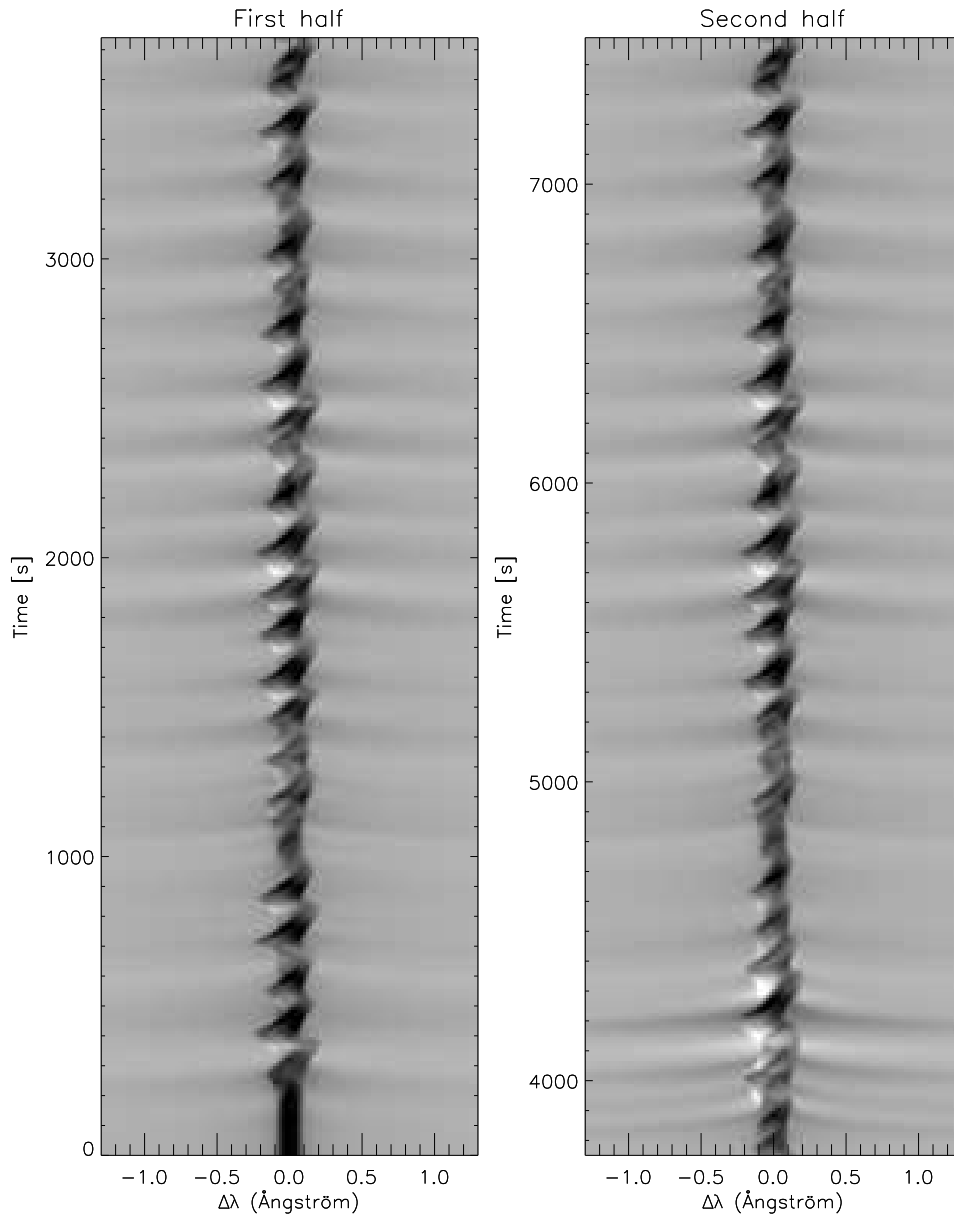


Fig. 15. The computed Ca II H line intensity as a function of wavelength for the full 7500s of the simulation. The piston velocities repeat after 3750s and one vertical position in the two panels thus have the same piston velocity. The pattern is almost identical in the two sections of the simulation outside the first startup periods.

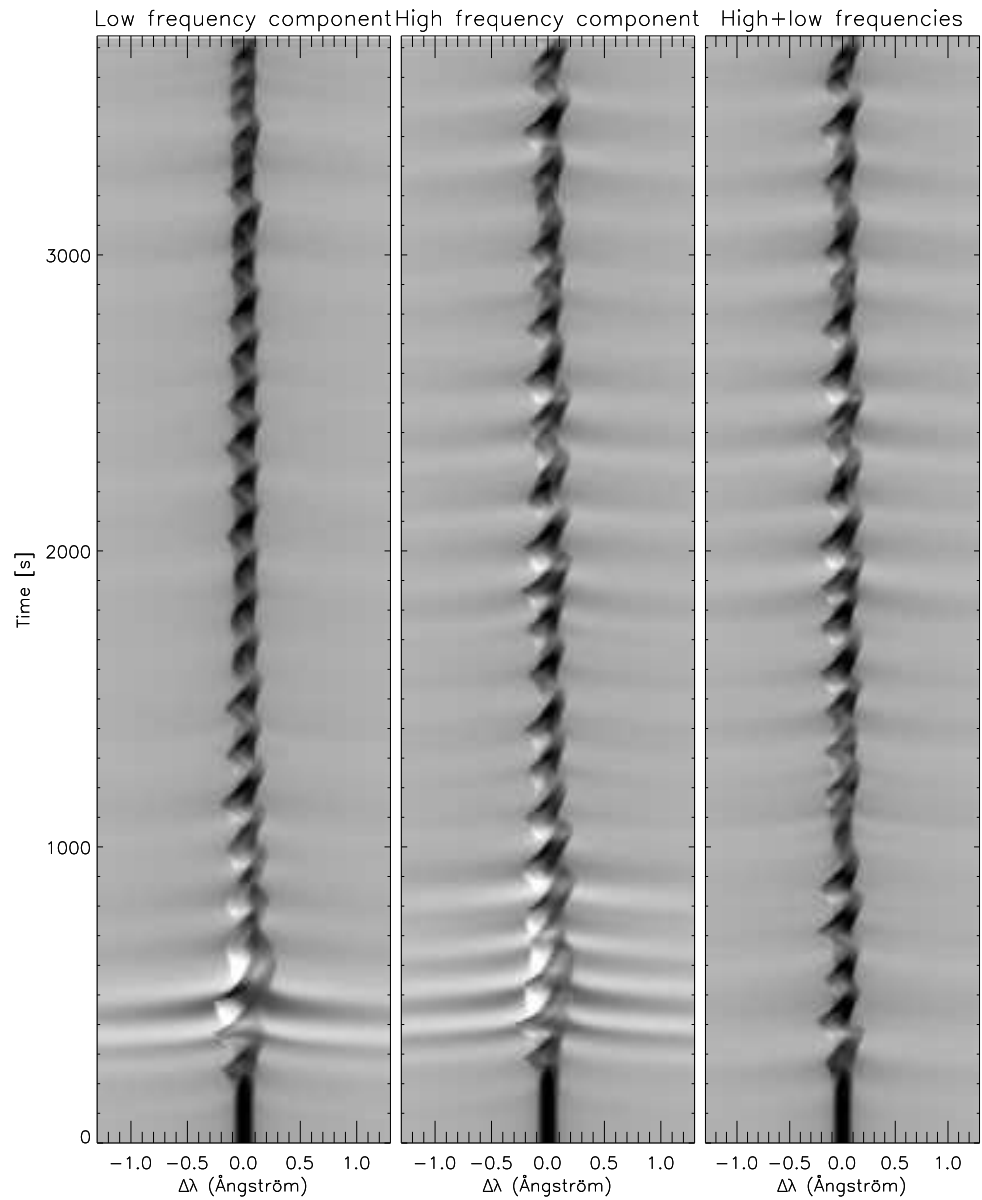


Fig. 16. The computed CaII H line intensity as a function of wavelength and time for three simulations. The right panel shows the first half of the full simulation while the other panels show simulations where the piston velocities have been low-pass or high-pass filtered at 4.5 mHz. The low frequency component simulation is shown in the left panel, the high frequency component simulation in the center panel.

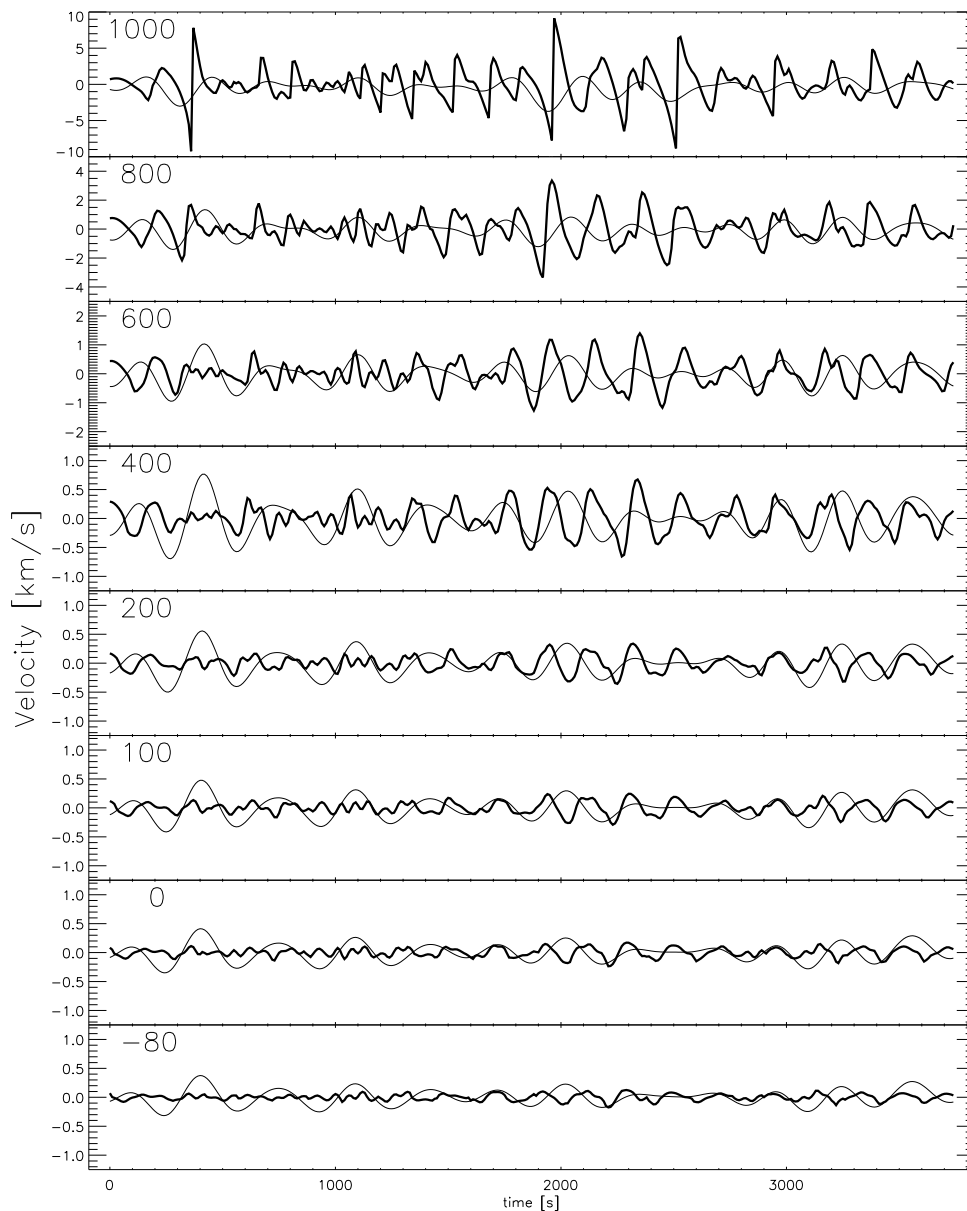


Fig. 17. Velocity as a function of time and height of the atmosphere. The height in km is indicated in the upper left corner of each panel. The velocity has been split into the frequency component below 4.5 mHz (thin) and the high frequency component above 4.5 mHz (thick). The bulk velocity is the sum of the two components. Note that the axis range is different for the top three panels. Strong grains in Fig 15 are clearly correlated with times of large high frequency velocity amplitudes at 1 Mm.

4. Discussion

Maybe the most important limitation of the simulations is the 1D restriction of horizontal homogeneity. The energy is forced to travel vertically, there is no radiative loss horizontally and there is no interference between velocities from different spatial points. All these effects can be expected to be important to the physics of the solar chromosphere but a self-consistent non-LTE radiative hydrodynamic simulation in more than one dimension is currently outside the computational possibilities. The observed spatial extent of bright grains is a few arcseconds similar to the total vertical extent of the simulation. A 1D description can therefore be expected to show some resemblance to the real sun, a view supported by the close resemblance of the simulations to observations of high spatial resolution. We thus feel that we can learn something about the real sun from the simulations but warn against over-interpretations.

The simulations aim at describing the non-magnetic internetwork regions of the sun. At some height this distinction between non-magnetic and magnetic regions has to break down with the spreading of the magnetic fields. Such a canopy has not been included in the simulations and for large heights one has to be increasingly careful with comparisons with observations. Reflections from hot material contained in magnetic regions above the internetwork may also influence the non-magnetic regions we aim at simulating.

The simulations were done neglecting the effects of line-blanketing. This will certainly affect the non-LTE statistical equilibrium of our diagnostic continua (UV overionization will be reduced) and the time variation of the radiation temperatures. We do not, however, expect a large effect on the deduced semi-empirical temperature structure based on the fact that both non-LTE and LTE modeling of the diagnostic continua result in the same semi-empirical model atmosphere. The neglect of line-blanketing will also affect the temperature structure in the upper photosphere in the initial model and also the amount of radiative damping and therefore the transfer function of the atmosphere. The neglect of cooling from CO has similar effects.

The transfer function of the atmosphere is furthermore affected by our treatment of the dynamic response of the convective flux divergence. We have assumed a constant convective energy flux divergence per gram on a Lagrangian scale. Based on inspections of 3D simulations of convection (Stein & Nordlund 1993, private communication) this is a reasonable approximation.

The limited numerical resolution will especially affect higher frequencies. The adaptive grid moves grid-points into shock regions but the resolution of waves starting to develop is limited. At the height of the piston the distance between grid-points is 1 km, increasing to 20 km above 300 km height. With ten points per wavelength, this corresponds to a maximum frequency of waves resolved everywhere of 30 mHz, and the numerical resolution should thus not much affect the high frequency waves before they start to shock.

The upper boundary condition aims at being transparent. During the timespan of the simulation, significant mass flows out of the boundary (after 7500 seconds $4 \times 10^{-4} \text{ g cm}^{-2}$). This has been taken into account by increasing the column mass of the top point correspondingly but no effect has been included on the pressure. The mass above the computational domain is thus not supported by the atmosphere in

the simulation. The outflow matter is also assumed to be transparent; no additional opacity is added in. A study of the effects of these assumptions on the results is being carried out.

Complete redistribution (CRD) has been assumed for all transitions. The Ca II H and K profiles will be affected by the neglect of partial redistribution (PRD). Details in the computed profiles, especially peak intensities and the inner wing intensity, should therefore be treated with caution. A proper PRD treatment would involve angle dependent redistribution. Such a study is planned.

Long timescales for ionization/recombination were neglected for all elements not treated self-consistently in the dynamic simulation (all important opacity contributors except hydrogen). One would expect these effects to give increased recombination behind shocks leading to a smaller amplitude for the radiation temperature variations with time. A general increased mean intensity could also be the result giving a higher semi-empirical temperature.

5. Conclusions

One main result is that the observed enhanced emission in magnetic field free inter-network regions can be produced by temporally varying waves that generate short intervals of high temperatures, without any increase in the average temperature structure. Because of the exponential dependence of the Planck function on temperature in the ultra-violet, although non-LTE source functions exhibit less sensitivity, these short intervals of high temperature dominate the time averaged intensity. Hence, the radiation temperature represents preponderantly the peaks in the gas temperature rather than its mean value. Because of this non-linear dependence of the Planck function on temperature, the radiation temperature of the mean intensity in the UV is more than the average of the radiation temperature. In addition, non-LTE effects can either increase or decrease the magnitude of intensity fluctuations compared to the magnitude of the temperature fluctuations.

The extra energy that is radiated away in the observed emission comes primarily from the energy dissipated by the wave motions, which goes directly into radiation without passing through a mediating state of enhanced mean thermal energy. The gas pressure work, PdV , goes primarily into changes in internal energy and gravitational energy.

Significant differences exist between hydrostatic model atmospheres and the average state of a dynamic atmosphere. The contribution function for the intensity in a dynamic atmosphere may be bimodal with one peak around $\tau_\nu=1$ and another at a shock at smaller optical depth. The mean height of formation will then be between those regions and have no relation to either formation region. Therefore, static formation heights and contribution functions can not be used for analyzing observations of chromospheric continua and lines. The source function is more and more decoupled from the local Planck function the higher in the atmosphere the continuum is formed. This means that the source function shows much less variation in time than the local temperature. Due to the non-LTE decoupling and also because of the width of the contribution functions, the emergent intensity does not show the discontinuous rise signature of shock waves even for the continua formed

where the shocks are strong.

Above the photosphere, the source function is so decoupled from the Planck function that variations in intensity can *not* be taken as a proxy for gas temperature variations. Even in the photosphere such a one-to-one correspondence between intensity variation and gas temperature variation is not possible because the formation height depends on the opacity and therefore on the temperature.

The modification of velocity amplitude and phase as a function of frequency and depth in the atmosphere can be described with a transfer function. This function is rather insensitive to the input velocity field up to heights of a few hundred kilometers but depends on the physics included in the model such as the treatment of line-blanketing and the treatment of the dynamic response of convective energy transport. Evanescent modes are strongly damped while higher frequencies are relatively undamped. By using the derived transfer function it is possible to construct piston velocities that give velocities higher in the atmosphere that match observed Doppler shifts rather well.

The simulations closely match the observed behaviour of CaII H₂V bright grains down to the level of individual grains. The asymmetry of the line profile is due to velocity gradients near 1Mm above where $\tau_{500}=1$. Regions with high opacity and a large source function (and therefore high emissivity) are Doppler shifted to frequencies where there is little matter above to absorb the radiation. The corresponding red peak is absent because of small opacity at the source function maximum. The brightness of the violet peak depends on the height of shock formation; if waves propagate into strongly downfalling matter this formation height may be below 1Mm where the high densities will cause strong emission. The position in wavelength of the bright violet peak depends on the bulk velocity at the shock peak and the width of the atomic absorption profile (described with the microturbulence fudge parameter).

The grain pattern is completely set by the velocity pattern of the piston. When the piston velocity pattern is repeated, the grain pattern also repeats. Both photospheric modes above and below the cut-off frequency influence the grain pattern but photospheric waves around 3 minute period were found to be most important. The grain pattern correlates with the velocity pattern at 1Mm. This velocity pattern is set by interference between different components at lower heights that propagate with different phase speeds until the shock formation heights.

Acknowledgements. The discussions at the mini-workshop in June inspired many improvements in the simulations and the computations described in this work were thus carried out after the mini-workshop. Lites and Rutten are thanked for making available their observations. This work was supported by a grant from the Norwegian Research Council and by grant NAGW-1695 from the National Aeronautics and Space Administration. The computations were supported by a grant from the Norwegian Research Council, tungregneutvalget.

References

- Carlsson, M.: 1986, *A Computer Program for Solving Multi-Level Non-LTE Radiative Transfer Problems in Moving or Static Atmospheres*, Report No. 33, Uppsala Astronomical Observatory
- Carlsson, M. and Stein, R. F.: 1992, *ApJ Let* **397**, L59
- Dorfi, E. A. and Drury, L. O.: 1987, *J. Comput. Phys.* **69**, 175
- Fontenla, J. M., Avrett, E. H., and Loeser, R.: 1993, *Astrophys. J.* **406**, 319
- Gustafsson, B.: 1973, *Uppsala Astr. Obs. Ann.* **5**, No. 6

- Kalkofen, W., Rossi, P., Bodo, G., and Massaglia, M.: 1992, in M. S. Giampapa and J. A. Bookbinder (Eds.), *Seventh Cambridge Workshop on Cool Stars, Stellar Systems and the Sun*, Astron. Soc. Pac. Conf. Series, Vol. 26, p. 543
- Lites, B. W., Rutten, R. J., and Kalkofen, W.: 1993, *Astrophys. J.* **414**, 345
- Mathisen, R.: 1984, *Oslo Inst. Theor. Astrophys. Publ. Series* **1**, 1
- Rammacher, W. and Ulmschneider, P.: 1992, *Astron. Astrophys.* **253**, 586
- Rossi, P., Kalkofen, W., Bodo, G., and Massaglia, S.: 1992, in M. Giampapa and J. M. Bookbinder (Eds.), *Cool Stars, Stellar Systems and the Sun*, Proc. Seventh Cambridge Workshop, Astron. Soc. Pac. Conf. Series, 26, p. 546
- Rutten, R. J. and Uitenbroek, H.: 1991, *Solar Phys.* **134**, 15
- Scharmer, G. B.: 1981, *Astrophys. J.* **249**, 720
- Scharmer, G. B. and Carlsson, M.: 1985, *J. Comput. Phys.* **59**, 56
- Seaton, M. J., Yan, Y., Mihalas, D., and Pradhan, A. K.: 1994, *Mon. Not. R. Astron. Soc.* **266**, 805
- Skartlien, R.: 1994, *Dynamics in stellar chromospheres*, Cand. Scient. Thesis, Inst. Theor. Astrophys. Oslo
- van Leer, B.: 1977, *J. Comput. Phys.* **23**, 276
- Vernazza, J. E., Avrett, E. H., and Loeser, R.: 1973, *Astrophys. J.* **184**, 605
- Vernazza, J. E., Avrett, E. H., and Loeser, R.: 1976, *Astrophys. J. Suppl. Ser.* **30**, 1
- Vernazza, J. E., Avrett, E. H., and Loeser, R.: 1981, *Astrophys. J. Suppl. Ser.* **45**, 635